Helicity-dependent terahertz emission spectroscopy of topological insulator Sb_2Te_3 thin films

Chien-Ming Tu,[1,2,3,*] Yi-Cheng Chen,[1] Ping Huang,[1] Pei-Yu Chuang,[4] Ming-Yu Lin,[4] Cheng-Maw Cheng,[5] Jiunn-Yuan Lin,[6] Jenh-Yih Juang,[1] Kaung-Hsiung Wu,[1] Jung-Chun A. Huang,[4,7,†] Way-Faung Pong,[2] Takayoshi Kobayashi,[1,8,9] and Chih-Wei Luo[1,7,‡]

[1]*Department of Electrophysics, National Chiao Tung University, Hsinchu, Taiwan 300, Republic of China*

[2]*Department of Physics, Tamkang University, New Taipei City 25137, Taiwan, Republic of China*

[3]*Department of Physics, Lund University, P.O. Box 118, SE-221 00 Lund, Sweden*

[4]*Department of Physics and Advanced Optoelectonic Technology Center, National Cheng Kung University, Tainan 701, Taiwan, Republic of China*

[5]*National Synchrotron Radiation Research Center, Hsinchu, Taiwan 300, Republic of China*

[6]*Institute of Physics, National Chiao Tung University, Hsinchu, Taiwan 300, Republic of China*

[7]*Taiwan Consortium of Emergent Crystalline Materials, Ministry of Science and Technology, Taipei 10601, Taiwan, Republic of China*

[8]*Advanced Ultrafast Laser Research Center and Department of Engineering Science, The University of Electro-Communications, Chofugaoka 1-5-1, Chofu, Tokyo 182-8585, Japan*

[9]*Japan Science and Technology Agency, Core Research for Evolutional Science and Technology (CREST), Japan Science and Technology Agency, K's Gobancho, 7, Gobancho, Chiyoda-ku, Tokyo 102-0076, Japan*

(Received 31 January 2017; revised manuscript received 9 October 2017; published 6 November 2017)

We report on helicity-dependent terahertz emissions that originate from the helicity-dependent photocurrents in topological insulator Sb_2Te_3 thin films due to ultrafast optical excitation. The polarity of the emitted terahertz radiation is controlled by both the incident angle and the helicity of optical pulses. Using an unprecedented decomposition-recombination procedure in the time domain, the signals of the Dirac fermions are fully separated from bulk contributions. These results provide insights into the optical coupling of topological surface states and open up opportunities for applying helicity-dependent terahertz emission spectroscopy in spintronics.

DOI: 10.1103/PhysRevB.96.195407

I. INTRODUCTION

Recently, the exotic properties of topological surface states (TSSs) in three-dimensional topological insulators (TIs) have attracted much attention due to their potentials in the applications of spintronics [1–5]. TSSs have been confirmed using several techniques, such as angle-resolved photoemission spectroscopy (ARPES) [4–6] and scanning tunneling microscopy [7–10], etc. In terms of the optical coupling of TSSs, it has been demonstrated that the helicity-dependent photocurrent originating from TSSs can be manipulated by the optical helicity and these results demonstrate the potential for optoelectronic devices based on the TSSs of TIs [11–16]. However, these results alone are inadequate to fully unveil the intriguing characteristics of TSS-photon coupling because of the limitations of indispensable electrodes in transport measurements and, in particular, the effects of TIs' crystalline orientation on photocurrents and the large signal background from thermoelectric currents. To address these problems, contact-free techniques have been proposed as viable alternatives. Terahertz emission spectroscopy is a useful contact-free technique for spintronics. For instance, transient spin currents [17] and photocurrents [18] that are generated by optical pulses on magnetic heterostructures have been recently studied by using terahertz emission spectroscopy.

Here, we demonstrate the observation of helicity-dependent terahertz emissions that originate from helicity-dependent photocurrents in TI Sb_2Te_3 thin films. Using the time-domain decomposition and recombination of the terahertz signals, the time-domain traces of the circular photogalvanic effect (CPGE), the linear photogalvanic effect (LPGE), and the photon drag effect (PDE) coefficients are extracted individually. It is worth noting that both the CPGE and the LPGE show similar characteristics in both the time and frequency domains and their polarities are coincident with the rotational symmetry of the Dirac cone of TIs. Furthermore, the anisotropic PDE is also clearly identified by the unique analysis as well as direct measurements.

II. EXPERIMENTS

Optical pulses with a central wavelength of 800 nm and a pulse duration of ∼75 fs were focused on the (111) surface of a Sb_2Te_3 thin film to generate terahertz radiation, as shown schematically in Fig. 1(a). The Sb_2Te_3 samples with 45-nm thickness were grown on $(1\bar{1}02)$ sapphire substrates by using molecular beam epitaxy, and the TSSs are clearly observed by using ARPES, as shown in Fig. 1(c). The details of sample preparation and the terahertz emission measurement are discussed in Appendix A. When circularly polarized optical pulses excite the Sb_2Te_3 thin films at an incident angle θ, an asymmetric distribution is generated in a helical Dirac cone because of the selection rules for Dirac fermions. Hot carriers are also generated and annihilate via relaxation processes on a picosecond time scale [19–23]. For TSSs, in-plane helicity-dependent photocurrents are generated in the direction (along the x axis) perpendicular to the plane of incidence [11–13] and radiate helicity-dependent terahertz emissions. Upon reversing the helicity of incident optical pulses, the direction of the helicity-dependent photocurrents is also reversed. Therefore, the polarity reversal of the emitted

*cmtu0813@gmail.com
†jcahuang@mail.ncku.edu.tw
‡cwluo@mail.nctu.edu.tw

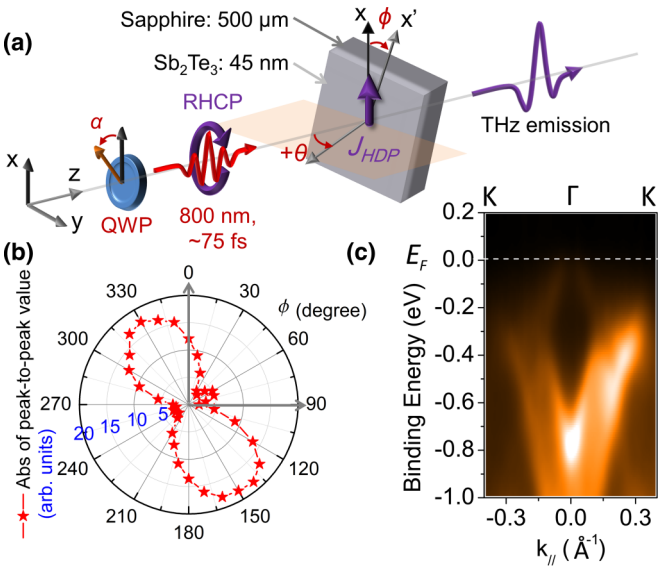

FIG. 1. (a) Right-hand circularly polarized (RHCP) optical pulses illuminate a topological insulator Sb_2Te_3 thin film at an incident angle $+\theta$ and generate a helicity-dependent photocurrent in the direction perpendicular to the incident plane (y-z plane). The polarization of optical pulses is controlled by rotating a quarter-wave plate (QWP) with an angle α. (b) The crystal-orientation-dependent (ϕ-dependent) absolute peak-to-peak amplitude of terahertz emission waveforms with linear polarization of optical pulses (along the x axis, $\alpha = 0°$) at nearly normal incidence ($\theta \sim +1°$). (c) The ARPES image of a used sample in this study. The Fermi level is denoted as E_F.

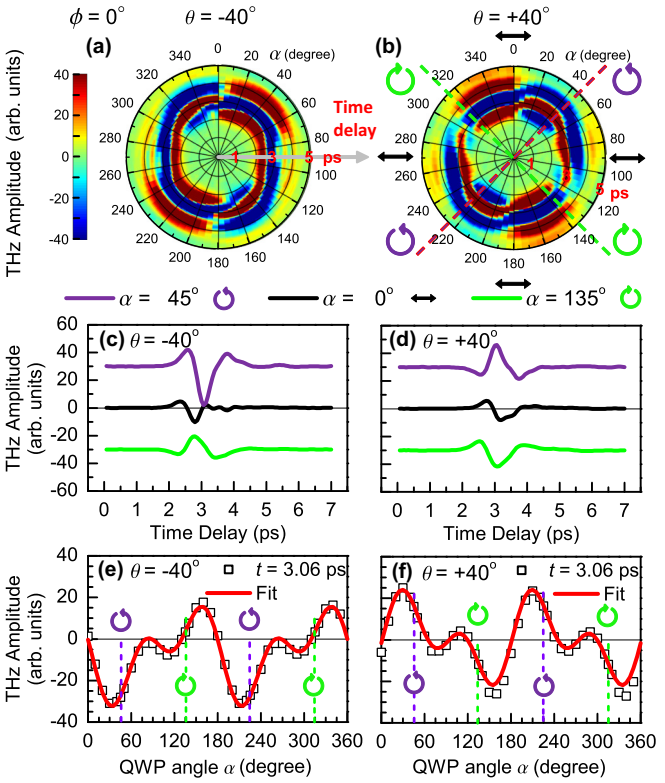

FIG. 2. (a), (b) Polar plots of terahertz waveforms (0–5 ps) as a function of α at $\theta = -40°$ and $+40°$, respectively, for $\phi = 0°$. The colors represent the amplitude of the terahertz emissions, (c), (d) Terahertz waveforms for excitation with linearly polarized, right-hand circularly polarized, and left-hand circularly polarized optical pulses at $\theta = -40°$ and $+40°$, respectively. (e), (f) The α-dependent terahertz amplitude at $t = 3.06$ ps. The red solid lines are the best fits with Eq. (1). The symbol ↔, the counterclockwise arrow, and the clockwise arrow denote linearly polarized (black: $\alpha = 0°$, along the x axis), right-hand circularly polarized (purple: $\alpha = 45°$), and left-hand circularly polarized (green: $\alpha = 135°$) incident photons, respectively.

terahertz pulses can be observed. The helicity-dependent effect scales with the incident angle θ, and it can be confirmed by changing the incident angle from $+\theta$ to $-\theta$ and vice versa.

The out-of-plane (i.e., perpendicular to the surface of TIs) bulk transient currents near the surface of TIs might contribute to terahertz emissions [24,25], and these can be avoided by polarization settings of terahertz detection (see Appendix A). In TIs, terahertz emissions originating from optical rectification (OR) have been observed recently [24–26]. In this study, we used linearly polarized (along the x axis) optical pulses to generate terahertz radiation from the Sb_2Te_3 thin films. As shown in Fig. 1(b), the azimuthal-scan (ϕ-scan) results for the peak-to-peak terahertz amplitudes of the terahertz emissions show twofold symmetry.

III. RESULTS AND DISCUSSION

The helicity-dependent terahertz emissions were characterized by rotating a quarter-wave plate (QWP) with an angle α at different incident angles θ, as shown in Fig. 2. The α-scan measurements along different crystalline orientations of TIs give more profound insights into the origins of terahertz emissions. According to the results for OR that are shown in Fig. 1(b), two orientations are selected: $\phi = 0°$ and 90° (see Appendix B). Figures 2(a) and 2(b) show the polar plots of terahertz waveforms (0–5 ps) for different-helicity optical excitations (α scan) at $\theta = -40°$ and $+40°$, respectively, for $\phi = 0°$. Twofold symmetries are clearly observed in the α-scan patterns. This phenomenon becomes more pronounced as the incident angle θ increases.

Figures 2(c) and 2(d) show that the time-domain terahertz waveforms from the Sb_2Te_3 thin film are generated by linearly polarized (LP, $\alpha = 0°$), right-hand circularly polarized (RHCP, $\alpha = 45°$), and left-hand circularly polarized (LHCP, $\alpha = 135°$) optical excitations. The polarity of the emitted terahertz radiation is reversed because the photon helicity is reversed. Furthermore, for helicity-fixed optical excitation (both RHCP and LHCP), the polarity reversal also occurs when the incident angle alternates from $+40°$ to $-40°$. These results are consistent with the scenario for the helicity-dependent terahertz emission: The spin-polarized current that is generated by incident photon spin is the main contributor to the process.

In terms of the optical control of TSSs, helicity-dependent photocurrents that are generated by optical pulses in TIs have been reported [11–13] and these are described as $J_{HDP}(\alpha) = C\sin(2\alpha) + L_1\sin(4\alpha) + L_2\cos(4\alpha) + D$, where C is the coefficient of the helicity-dependent CPGE and L_1 describes the helicity-independent LPGE. Both C and L_1 are related to the TSSs, and it has been theoretically predicted that both the CPGE and LPGE are linked by the Berry phase in spin-orbit coupled quantum well structures [27]. Macroscopically, both the CPGE and LPGE can be

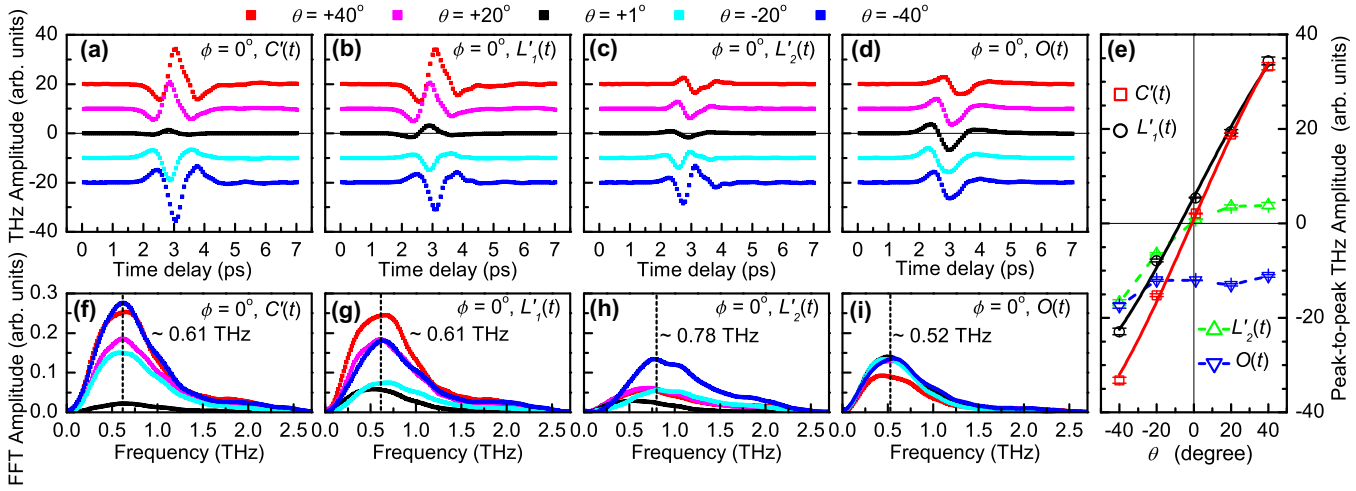

FIG. 3. (a)–(d) The time-domain traces for the coefficients $C'(t)$, $L'_1(t)$, $L'_2(t)$, and $O(t)$ are extracted [using Eq. (1)] individually from the α-dependent terahertz amplitudes with various time delays t at $\phi = 0°$. In (a)–(d), all data are offset to ensure greater clarity. (f)–(i) The corresponding spectra of the time-domain traces in (a)–(d) by FFT. (e) The peak-to-peak terahertz amplitude of the time-domain traces in (a–d) as a function of the incident angle θ. The red and black lines are the best sinusoidal fits for $C'(t)$ and $L'_1(t)$, respectively.

described by third-rank tensors [11,14,28–30]. Both of them require the electric-field component of incident light in the direction of the sample's surface normal and are odd in the incident angle θ [14,28,30]. L_2 describes the PDE and the bulk thermoelectric current contributes to D. The PDE can be described by a fourth-rank tensor and is associated with the linear momentum transfer between incident photons and electrons. In terms of the transient current, the terahertz electric field is described as $E_{\mathrm{THz}}(\alpha,t) \propto \partial J_{\mathrm{HDP}}(\alpha,t)/\partial t$. OR also contributes to the terahertz emissions. Therefore, the helicity-dependent terahertz emission from TIs is described as follows:

$$E_{\mathrm{THz}}(\alpha,t) \propto C'(t)\sin(2\alpha) + L'_1(t)\sin(4\alpha) + L'_2(t)\cos(4\alpha) + O(t). \quad (1)$$

The coefficient $C'(t)$ describes the terahertz radiation that originates from the helicity-dependent CPGE. $L'_1(t)$ and $L'_2(t)$ are the coefficients for the LPGE and the PDE, respectively. OR mainly contributes to $O(t)$. OR is a second-order nonlinear-optical process, and the nonlinear polarization of OR follows the time dependents of the incident light intensity [31]. Full descriptions about the dependences of CPGE, LPGE, PDE, and OR on ϕ, θ, and α are shown in Appendix C. To test this model, we use Eq. (1) to fit the experimental data by choosing the specific moment at which the α-dependent terahertz amplitude shows the largest variation. Figures 2(e) and 2(f) show the time-domain fits for the α scans [Figs. 2(a) and 2(b)] with a time delay $t = 3.06$ ps at $\theta = -40°$ and $+40°$, for $\phi = 0°$. Obviously, Eq. (1) fits the experimental results very well, and the polarity reversals are significant at the chosen moment. The time-domain traces are also produced for all coefficients and the results are discussed in detail later.

The separation of the signals due to the Dirac fermions from the massive bulk contributions in topological insulators is an important concern in modern condensed matter physics. ARPES measurements have successfully achieved this goal and the dynamics of Dirac fermions are also obtained by using a time-resolved ARPES technique [20,21,32]. To achieve a similar goal, we develop a method that is suitable for extracting all coefficients based on Eq. (1) for every time delay and separating the signals of the Dirac fermions from the other bulk contributions. Figures 3(a)–3(d) show the time-domain traces of the coefficients $C'(t)$, $L'_1(t)$, $L'_2(t)$, and $O(t)$, which are extracted individually from different α scans, for $\phi = 0°$, and all data are offset to ensure greater clarity. Comparing Fig. 3(a) with Fig. 3(b), all of the extracted time-domain traces for the coefficients $L'_1(t)$ show similar characteristics to those for the coefficients $C'(t)$. When the incident angle θ changes its sign, the polarities of the time-domain traces for both $C'(t)$ and $L'_1(t)$ change correspondingly. In the fast-Fourier-transform (FFT) spectra of $C'(t)$ and $L'_1(t)$ [Figs. 3(f) and 3(g)], the peaks for all of the spectra are located at ~0.61 THz, which is in very good agreement with the results for the time-domain analysis. These results strongly indicate that both $C'(t)$ and $L'_1(t)$ share the same physical origin.

It is also worth noting that the amplitude of the time-domain traces evolves with the incident angle θ. Taking into account the Fresnel coefficient and the procedure for optical-fluence normalization, Fig. 3(e) shows the calibrated peak-to-peak terahertz amplitudes for all traces in Figs. 3(a)–3(d) as a function of θ. It is obvious that the sign for the peak-to-peak terahertz amplitudes of both $C'(t)$ and $L'_1(t)$ changes when the sign of θ changes. The best fit for $C'(t)$ (red line) almost intersects the origin and this result is consistent with the characteristics of CPGE: The photon spin is orthogonal to the two-dimensional spin texture of the Dirac cone at normal incidence. For $L'_1(t)$ (black line), an offset is seen at $\theta = +1°$, which may be caused by OR. Although the sign change can also be observed for $L'_2(t)$ in Fig. 3(e), the polarity reversal seems to be difficult to identify in Fig. 3(c). This might be due to the interferences from OR. On the contrary, at $\phi = 90°$, the polarity reversal features of the PDE are not only clearly observed in time-domain analysis (see Appendix C) but are also revealed by the direct measurements.

The photon drag effect has been observed in graphene by using terahertz emission spectroscopy [33]. In previous reports

of photocurrent measurements [11–13], the coefficient $L'_2(t)$ associated with the PDE describes the experimental results well but PDE has only been confirmed by a recent terahertz-laser-driven experiment [34]. In this study, the anisotropic PDE is not only directly measured by linear-polarized optical excitation but also demonstrated by the time-domain recombination of $L'_2(t) + O(t)$ at $\phi = 90°$. As shown in Fig. 4(a), the polarity of the time-domain terahertz waveforms that are generated by linear-polarized ($\alpha = 0°$) optical pulses changes when the sign of the incident angle θ changes from $+40°$ to $-40°$, which is direct evidence of PDE. Figure 4(d) shows the FFT spectra for the directly measured terahertz waveforms that are shown in Fig. 4(a). The peaks for all of the spectra are located at a frequency of ~0.73 THz.

We also observe similar evidences in time-domain decomposition and recombination of the α scans at $\phi = 90°$ (see Appendix D). As mentioned previously, OR can affect other helicity-independent terms and can have some residual contribution to the $L'_2(t)$ and O(t) terms in the normal incidence case ($\theta = +1°$). It is worth emphasizing that these residuals are opposite in sign. Therefore, the time-domain traces of $L'_2(t)$ and O(t) are combined together, as shown in Fig. 4(b). A comparison of Figs. 4(a) and 4(b) shows that the combined traces of $L'_2(t) + O(t)$ are almost the same as the directly measured terahertz waveforms at $\alpha = 0°$. The

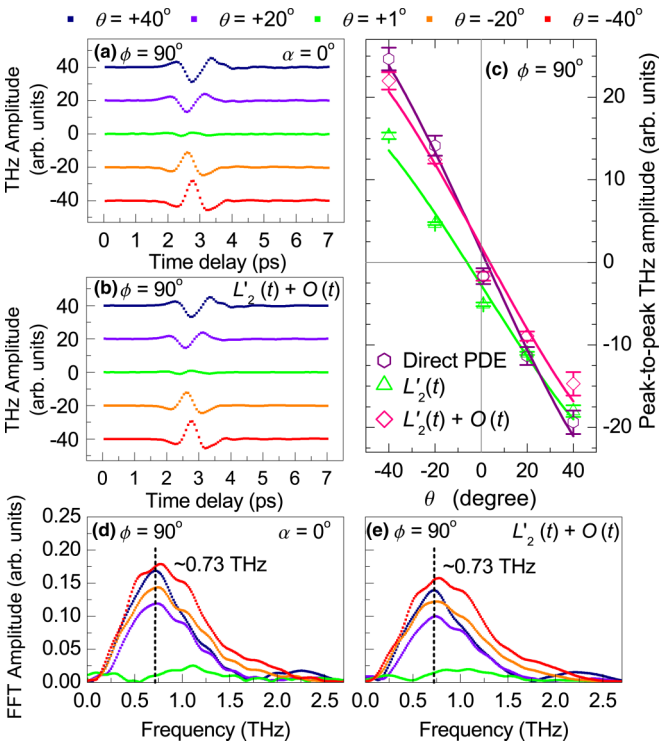

FIG. 4. (a) The terahertz emissions are generated using linearly polarized ($\alpha = 0°$) optical pulses at various incident angles from $\theta = -40°$ to $+40°$, at $\phi = 90°$. (b) The combination of the time-domain traces $L'_2(t)$ and $O(t)$ at $\phi = 90°$ (see Appendix D). (d), (e) The corresponding spectra of the time-domain traces in (a), (b) by FFT. (c) The peak-to-peak terahertz amplitudes of the terahertz emissions from direct PDE in (a) (purple hexagons), $L'_2(t) + O(t)$ (pink diamonds), and $L'_2(t)$ (green triangles), as a function of the incident angle θ. The solid lines represent the best sinusoidal fits.

FFT spectra of $L'_2(t) + O(t)$ [in Fig. 4(e)], which has a peak at ~0.73 THz, also agree with that of the directly measured results in Fig. 4(d). In Fig. 4(c), all of the peak-to-peak terahertz amplitudes for the direct measurements (direct PDE), $L'_2(t)$ and $L'_2(t) + O(t)$, change their signs when the sign of θ changes. These are fitted well with the sinusoidal function. Obviously, the term $L'_2(t) + O(t)$ is much closer to the directly measured value than the $L'_2(t)$ term alone. These results not only verify the reliability of this time-domain analysis, but also prove that $L'_2(t)$ clearly represents the PDE.

A comparison of the time-domain decomposition and recombination for $\phi = 0°$ and $90°$ shows that all of the extracted time-domain traces of the coefficient $L'_1(t)$ behave similarly to that of the coefficient $C'(t)$. The polarities of the time-domain traces $C'(t)$ and $L'_1(t)$ at $\phi = 90°$ are the same as those at $\phi = 0°$, and their FFT spectra also have the same shape with a peak at ~0.59 THz (see Appendix D). All of these results are in good agreement with the rotational symmetry of the Dirac cone in TIs. Furthermore, in spin-orbit coupled quantum well structures, both CPGE and LPGE photocurrents associated with the Berry phase have been theoretically predicted to have equal magnitude [27]. In this study, the experimental results of the time-domain traces and the peak-to-peak analysis of both $C'(t)$ and $L'_1(t)$ are close at both $\phi = 0°$ and $90°$ [Fig. 3(e), and Fig. 8(e) (in Appendix D)]. The tendency in the experimental observations agrees with this theoretical prediction.

Recently, time-resolved ARPES measurement of Sb_2Te_3 single crystals has been reported [22]. An asymmetric distribution in the Dirac cone due to circularly polarized optical excitation has been confirmed and these results are coincident with the results for helicity-dependent photocurrents in the transport experiments [11,13]. Based on the time-resolved ARPES results and considering transient-current radiation and far-field diffraction [35,36], we simulate the terahertz emission waveforms and spectra from different positions in the TSSs (see Appendix E). The peaks of terahertz spectra are located at around 0.56–0.60 THz for the positions near the Dirac point. ($E - E_F < 0.3$ eV, Fig. 9(d) in Appendix E). These peak positions are coincident well with the peak positions of the $C'(t)$ and $L'_1(t)$ spectra for both $\phi = 0°$ and $90°$ [see Fig. 3, and Fig. 8 (in Appendix D)]. These results give strong evidence that the $C'(t)$ and $L'_2(t)$ originate from TSSs. Therefore, it can be expected that the photoexcited carriers near the Dirac point in the TSSs mainly contribute to the helicity-dependent terahertz emission from a TI Sb_2Te_3 under circularly polarized optical excitations.

Recently, some TI-terahertz-emission works based on circularly polarized excitation have been reported, and these works either use circular dichroism or single delay-time analysis [37,38]. Helicity-dependent terahertz emission measurements of Bi_2Se_3 thin films have been demonstrated, and a threefold periodicity with a constant offset in azimuthal scan has been observed [38]. This observation has been ascribed to circular photon drag effect, and the origin of the constant offset part is still unclear due to the limited information from experimental results and model fitting [38]. Regarding transient-current radiation, the frequency of few-cycle terahertz pulses are inversely proportional to the carrier relaxation time. Longer carrier relaxation times result in lower-frequency terahertz emissions. It is well known that the carrier relaxation times in

TSSs of the typical TIs, e.g., Bi_2Se_3 and Bi_2Te_3, are $\geqslant 10$ ps and are longer than those in the bulk states [21,23,32,39,40]. In the case of Bi_2Se_3, the carrier relaxation time in TSSs is ∼10 ps at 70 K [32], and the estimated frequency of the terahertz emissions from Bi_2Se_3 would be ∼0.1 THz, which is close to the results (∼0.23 THz) of Ref. [38]. For Sb_2Te_3 at room temperature, the carrier relaxation time in the TSSs is ∼1.2 ps from time-resolved ARPES results [22]. Therefore, the estimated frequency of the terahertz emissions from Sb_2Te_3 is ∼0.8 THz, which is consistent with our results of 0.61 THz for CPGE and LPGE in this study. The time-domain decomposition-recombination method developed in this study could be further applied to other TIs.

IV. SUMMARY AND CONCLUSIONS

In summary, we have demonstrated that the helicity-dependent terahertz emissions from topological insulator Sb_2Te_3 thin films can be manipulated by using ultrafast optical pulses. Using the time-domain decomposition and recombination, the terahertz waveforms that originate from the CPGE, the LPGE, and the PDE are extracted individually. Both the CPGE and the LPGE results agree with the rotational symmetry of the Dirac cone, as verified by different crystalline orientation measurements. Anisotropic PDE is also observed by both direct measurements using linearly polarized light and the time-domain decomposition-recombination analysis. Furthermore, the spectra of time-domain traces for the CPGE and the LPGE coefficients agree with the simulated terahertz spectra of the transient photoexcited carriers near the Dirac point, which are observed by using time-resolved ARPES. The observations of this study not only demonstrate the importance of field-resolved terahertz emissions, but also pave the way towards applications of helicity-dependent terahertz emission spectroscopy in spintronics.

ACKNOWLEDGMENTS

This work was supported by Ministry of Science and Technology, Taiwan (Grants No. 103-2119-M-009-004-MY3, No. 103-2628-M-009-002-MY3, and No. 106-2628-M-009 -003-MY3) and Ministry of Education through the Aiming for the Top University Program at National Chiao Tung University.

APPENDIX A: SAMPLE PREPARATION AND TERAHERTZ EMISSION MEASUREMENT

In this study, Sb_2Te_3 thin films were grown by using molecular beam epitaxy (MBE) on $(1\bar{1}02)$ R-plane sapphire substrates; in-plane mismatch is around 12%. The sapphire substrate was heated to 1000°C for 1 h to remove contaminants. High-purity Sb (99.999%) and Te (99.999%) were evaporated by Knudsen cells and the fluxes were calibrated *in situ* by using a quartz crystal microbalance. The base pressure for the MBE system was less than 1×10^{-10} Torr and the growth pressure for the Sb_2Te_3 thin films was maintained at less than 1×10^{-9} Torr. The Sb and Te effusion cell temperatures were selected so that the fluxing ratio Te/Sb was 12. The Sb deposition rate was 1 Å/min and that for Te was 12 Å/min. The substrate temperature was maintained at 230°C throughout the

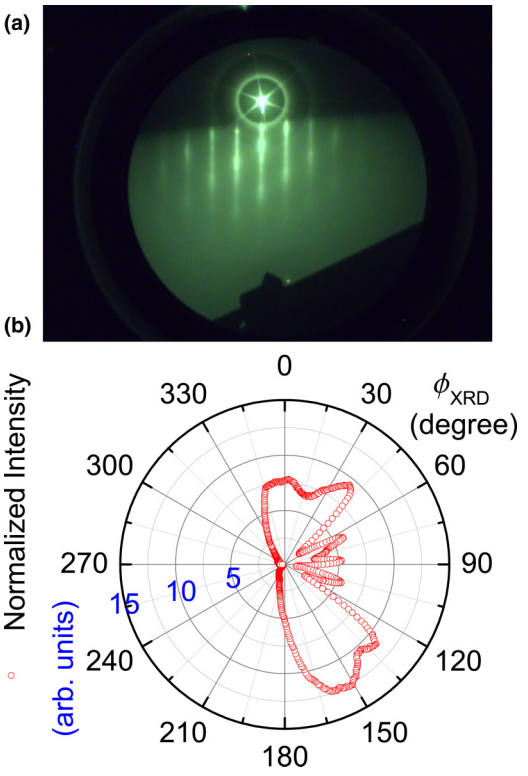

FIG. 5. (a) The *in situ* reflection high-energy electron diffraction (RHEED) pattern of the used Sb_2Te_3 thin film. (b) The x-ray diffraction ϕ-scan (ϕ_{XRD}) pattern of the Sb_2Te_3 thin film on a $(1\bar{1}02)$ R-plane sapphire substrate.

growth. The single-crystal structure of the film was obtained by using *in situ* reflection high-energy electron diffraction (RHEED), as shown in Fig. 5(a). The Sb_2Te_3 samples with 45-nm thickness were used for terahertz emission experiments, and a capping layer (∼10 nm) of Se was deposited on the surface of Sb_2Te_3 thin films to prevent oxidation or reaction with the TI thin films.

The crystal structure of R-plane sapphires is rectangle and it shows a twofold symmetry. Although the symmetry of Sb_2Te_3 (111) is hexagonal, the lattice mismatch between Sb_2Te_3 thin films and R-plane sapphire substrates may be induced during thin-film-growth process. Optical rectification (OR) is a second-order nonlinear optical process, and the ϕ-scan patterns of second-order nonlinear-optical effects strongly depend on the crystal structure of samples. We performed x-ray diffraction measurements on the samples. As shown in Fig. 5(b), the x-ray diffraction ϕ-scan (ϕ_{XRD}) pattern of a Sb_2Te_3 (111) thin film shows a twofold symmetry. This result is coincident with the OR-ϕ-scan pattern as shown in Fig. 1(b) in the main text.

In the terahertz emission experiments, a mode-locked Ti:sapphire oscillator was used to generate an optical pulse train with a central wavelength of 800 nm, a pulse duration of ∼75 fs, and a repetition rate of 5.1 MHz. Optical pump pulses illuminated the (111) surface of the TI thin films to generate terahertz radiation. The pulse energy of the pump beam was around 31.4 nJ and the spot size (diameter) on the surface of samples was about 450 μm at normal incidence. Therefore, the pump fluence was about 19.4 μJ/cm^2. The terahertz radiation

emitted from the sample was collimated by two off-axis parabolic mirrors and focused on a 1-mm-thick ⟨110⟩ ZnTe slab for electro-optic sampling. A wire-grid polarizer was used to purify the polarization of the terahertz radiation along the x axis (in-plane) and electro-optic sampling was also used to detect terahertz polarization along the x axis. All of the experiments were performed at room temperature and in a chamber purged by dry nitrogen gas, to avoid the absorption of water vapor. The helicity-dependent terahertz emissions were characterized by rotating a quarter-wave plate with an angle α (α scan). The rotation of the quarter-wave plate changes the photon polarization from linearly polarized ($\alpha = 0^\circ$), to right-hand circularly polarized ($\alpha = 45^\circ$), to linearly polarized ($\alpha = 90^\circ$), to left-hand circularly polarized ($\alpha = 135^\circ$), and to linearly polarized ($\alpha = 180^\circ$). This type of polarization change shows a period of 180°.

Firstly, we performed normal-incident excitation ($\theta = +1^\circ$ and linearly polarized pump beam) and rotated the samples over 360° (OR ϕ-scan) to determine the contributions from OR. At $\phi = 90^\circ$, the contributions of OR almost reach to zero, and this means that the terahertz emission generated by other mechanisms can be unambiguously identified along this crystalline orientation. In order to double-check our idea, the other ϕ angle of 0° [30° offset from the OR maximum in Fig. 1(b) of the main text] with a portion of the OR signal was selected for the same analyses as performed at $\phi = 90^\circ$. This offset of 30° between the OR maximum and $\phi = 0^\circ$ is just to avoid the large OR component and keep a reasonable amplitude of terahertz signal for the subsequent analyses. As shown in the main text, the time-domain traces and spectra of both $C'(t)$ and $L_1'(t)$ at $\phi = 0^\circ$ are really coincident with those at $\phi = 90^\circ$.

APPENDIX B: TIME-DOMAIN FITS FOR THE HELICITY-DEPENDENT TERAHERTZ RADIATION AT $\phi = 0^\circ$ AND 90°

Crystalline-orientation-dependent measurements can give a clearer insight into the origins of terahertz emissions. The α-scan patterns and the time-domain fits at different incident angles θ for $\phi = 0^\circ$ and 90° are shown in Figs. 6 and 7, respectively. At nearly normal incidence [$\theta = +1^\circ$, Figs. 6(g) and 7(g)] in both orientations, obviously, the α-scan patterns show clear fourfold symmetry and the main contributor is optical rectification (OR). By contrary, at oblique incidences ($\theta = -40^\circ$ and $+40^\circ$), for both $\phi = 0^\circ$ and 90°, the α-scan patterns show clear twofold symmetry and it means that the helicity-dependent circular photogalvanic effect (CPGE) affects the results. For the same incident angle, for example, $\theta = +40^\circ$, the α-scan patterns [Figs. 6(m) and 7(m)] are similar but not identical. It indicates that the anisotropic photon drag effect (PDE) contributes to the results and it is discussed later.

According to Eq. (1) in the main text, $E_{\mathrm{THz}}(\alpha,t) \propto C'(t)\sin(2\alpha) + L_1'(t)\sin(4\alpha) + L_2'(t)\cos(4\alpha) + O(t)$, we use this equation to fit the experimental data at different time delay. Apparently, Eq. (1) fits the experimental results very well at all incident angles for both $\phi = 0^\circ$ and 90°, as shown in Figs. 6 and 7.

In Figs. 2(d)–2(f) (see main text), the polarity reversals of the terahertz waveforms by right-hand circularly polarized (RHCP) and left-hand circularly polarized (LHCP) optical excitations are clearly demonstrated. However, the terahertz amplitudes for RHCP and LHCP optical excitations are not equal, as shown in Figs. 6 and 7. This means that other helicity-independent effects are also involved in the terahertz emissions, and only circularly polarized optical excitation would not be sufficient to disentangle the intrinsic underlying physical mechanisms.

APPENDIX C: DEPENDENCE OF CIRCULAR PHOTOGALVANIC EFFECT, LINEAR PHOTOGALVANIC EFFECT, PHOTON DRAG EFFECT, AND OPTICAL RECTIFICATION ON ϕ, θ, AND α

Macroscopically, the photocurrent J_λ generated by the electric field $\mathbf{E}$ of incident light is shown as follows [11,14,28–30]:

$$J_\lambda = \sum_\mu \gamma_{\lambda\mu} i(\mathbf{E}\times\mathbf{E})_\mu + \frac{1}{2}\sum_{\mu\upsilon}\chi_{\lambda\mu\upsilon}(E_\mu E_\upsilon^* + E_\upsilon E_\mu^*) + \sum_{\delta\mu\upsilon} T_{\lambda\delta\mu\upsilon} q_\delta E_\mu E_\upsilon^*,$$

where $\gamma_{\lambda\mu}$ is a third-rank pseudotensor for the CPGE. $\chi_{\lambda\mu\upsilon}$ is a third-rank tensor for the LPGE. $T_{\lambda\delta\mu\upsilon}$ is a fourth-rank tensor for the PDE. q_δ is the photon linear momentum. The indices run through the spatial coordinate.

The CPGE photocurrents change sign as the polarization of the incident light changes from the right-hand circular polarization to the left-hand circular polarization [29,30]. Therefore, the CPGE shows 2α periodicity. On the other hand, because the LPGE has no response to the changes in the helicity of the incident light as well as the second-order dependence on the electric field of the incident light, the LPGE shows 4α periodicity [14,30]. Macroscopically, both the CPGE and LPGE require the electric-field component in the direction of the sample's surface normal, and both of them are odd in the incident angle θ [28,14]. As the incident angle of light changes sign, e.g., from $+\theta$ to $-\theta$, with respect to the surface normal of a sample, the incident electrical-field component (in the direction of the surface normal) changes sign as well, and the direction of the LPGE photocurrent also reverses. Therefore, the time-domain traces of the LPGE flip.

In quantum well structures, it has been theoretically predicted that both CPGE and LPGE are linked by the Berry phase, and the Berry phase generates both PGEs with equal magnitude [27]. Microscopically, for TIs, the CPGE originates from the TSSs and satisfies the rotational symmetry of the Dirac cone [29]. Therefore, the CPGE should show the same characteristics at different crystal orientations. Nevertheless, a fully microscopic theory of the LPGE in TIs is still absent.

The PDE is described by a fourth-rank tensor $T_{\lambda\delta\mu\upsilon}$. It depends on not only photon linear momentum q_δ but also the polarization of incident light [14,28]. The main feature of the PDE is that its sign changes as the incident angle of the linearly polarized incident light reverses from $+\theta$ to $-\theta$. It may also show the anisotropic behaviors (i.e., ϕ dependent) because of the fourth-rank tensor.

OR is one of the second-order nonlinear-optical processes, and basically it is described by the third-rank nonlinear-optical tensor $\chi^{(2)}$ which is the same as the well-known second-harmonic generation in noncentrosymmetric materials

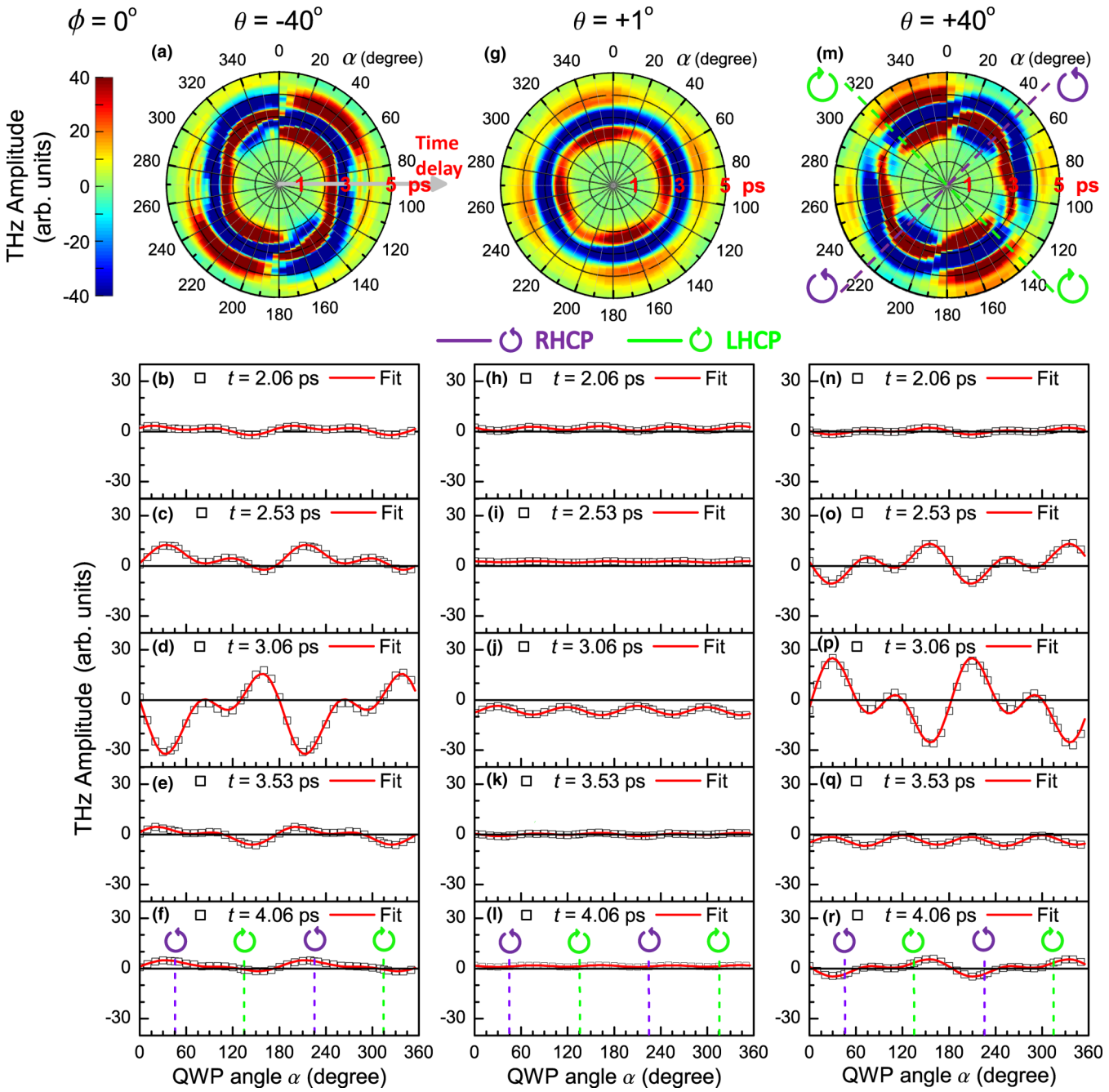

FIG. 6. $\phi = 0°$: (a) $\theta = -40°$, (g) $\theta = +1°$, and (m) $\theta = +40°$ as defined in the top panels. The top panels show the polar plots for the terahertz waveforms (0–5 ps). The colors represent the amplitude of the terahertz radiation. (b)–(f) For $\theta = -40°$, the time-domain amplitudes of the terahertz waveforms at $t = 2.06$, 2.53, 3.06, 3.53, and 4.06 ps are shown. The red solid lines are the fits to the data. The results for $\theta = +1°$ ($\theta = +40°$) are shown in (h)–(l) [(n)–(r)].

(i.e., $P^{\mathrm{OR}} = \varepsilon_0 \chi^{(2)} |E|^2$, P^{OR} is the nonlinear polarization of OR, and ε_0 is the electric permittivity of free space). This indicates that the nonlinear polarization P^{OR} of OR depends on the crystal orientation and the intensity profile of incident light [31]. Besides, both right-hand circular polarization and left-hand circular polarization of the incident light are identical in the OR process. Therefore, it shows 4α periodicity, and no polarity reversal for OR as the sign of the incident angle θ changes. The details of the dependences of CPGE, LPGE, PDE, and OR on ϕ, θ, and α are shown in Table I.

APPENDIX D: TIME-DOMAIN DECOMPOSITION AND RECOMBINATION OF THE α-DEPENDENT TERAHERTZ WAVEFORMS AT $\phi = 90°$

The time-domain decomposition-recombination procedure is also applied to the terahertz waveforms measured at $\phi = 90°$. At $\phi = 90°$, OR reaches almost zero, and this means that the terahertz emission generated by other mechanisms can be unambiguously identified along this crystalline orientation. In Figs. 8(a) and 8(b), all of the extracted time-domain traces of

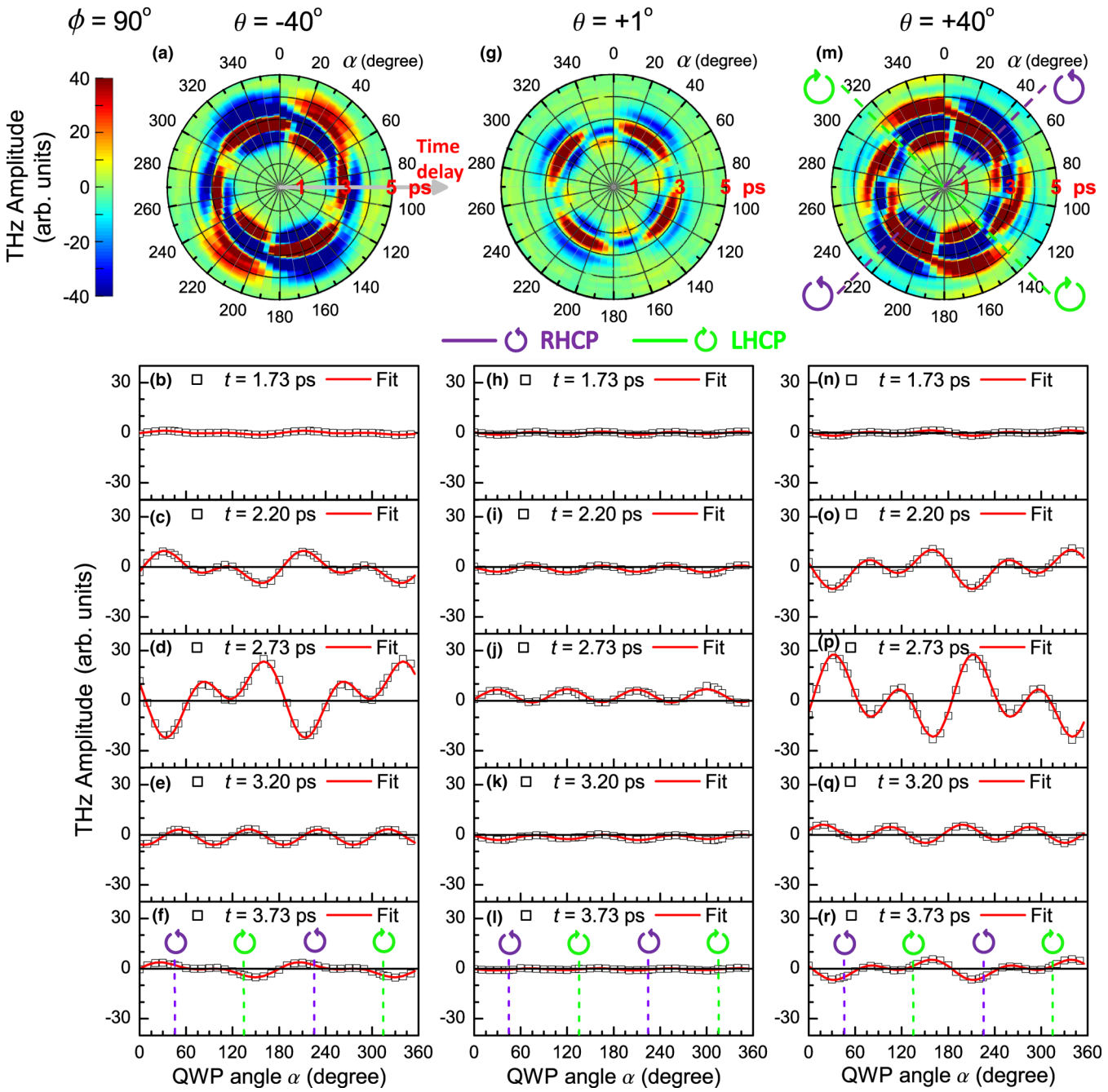

FIG. 7. $\phi = 90°$: (a) $\theta = -40°$, (g) $\theta = +1°$, and (m) $\theta = +40°$ as defined in the top panels. The top panels show the polar plots for the terahertz waveforms (0–5 ps). The colors represent the amplitude of the terahertz radiation. (b)–(f) For $\theta = -40°$, the time-domain amplitudes for the terahertz waveforms at $t = 1.73$, 2.20, 2.73, 3.20, and 3.73 ps are shown. The red solid lines are the fits to the data. The results for $\theta = +1°$ ($\theta = +40°$) are shown in (h)–(l) [(n)–(r)].

the coefficients $L_1'(t)$ show characteristics similar to that of the coefficients $C'(t)$. The fast-Fourier-transform (FFT) spectra for both $C'(t)$ and $L_1'(t)$ have the same shape with a peak at ~0.59 THz and this value is very close to that at $\phi = 0°$ (0.61 THz). As shown in Fig. 8(c), the polarity of the time-domain traces $L_2'(t)$ is reversed when the sign of the incident angle θ changes. This is the main feature for photon drag effect.

APPENDIX E: ESTIMATION OF THE TERAHERTZ-EMISSION SPECTRA FOR DIRAC FERMIONS BY USING PHOTOEMISSION DYNAMICS FROM TIME-RESOLVED ARPES MEASUREMENTS

Time-resolved ARPES measurements on TIs provide valuable insights into the carrier dynamics of TIs under circularly polarized optical excitation. Recently, direct optical transitions

TABLE I. Dependence of CPGE, LPGE, PDE, and OR on ϕ, θ, and α.

	ϕ: Crystalline orientation	θ: Incident angle ($\theta \rightarrow -\theta$)	α: QWP angle
CPGE	Macroscopic: $\gamma_{\lambda\mu}$ Microscopic: TSS[a] ϕ-Independent	Polarity: sign change	2α-Periodicity $\sin 2\alpha$
LPGE	Macroscopic: $\chi_{\lambda\mu\upsilon}$ Microscopic: TSS[a] ϕ-Independent	Polarity: sign change	4α-Periodicity $\sin 4\alpha$[b]
PDE	$T_{\lambda\delta\mu\upsilon}$ ϕ-Dependent	Polarity: sign change	4α-Periodicity $\cos 4\alpha$[c]
OR	$\chi^{(2)}$[d] ϕ-Dependent	Polarity: no sign change	4α-Periodicity $\cos 4\alpha$[e]

[a]Both CPGE and LPGE are linked by Berry phase in quantum well structures [27].
[b]The experimental results (time-domain traces and spectra) of $L_1'(t)$ show that the $\sin 4\alpha$ term is dominant and are coincident with those of $C'(t)$.
[c]The experimental results (time-domain traces and spectra) of $L_2'(t)$ show that the $\cos 4\alpha$ term is dominant and are coincident with those of the direct PDE.
[d]$\chi^{(2)}$: The second-order nonlinear-optical tensor [31].
[e]OR contributes mainly to the $\cos 4\alpha$ term, and it is confirmed by using a $\langle 110 \rangle$ ZnTe single crystal as a terahertz emitter through OR effect (see Fig. 10 in Appendix F).

from deeper-lying bulk states to TSSs in Sb_2Te_3 single crystals at room temperature have been observed [22]. Using circularly polarized optical pulses (800 nm, 1.55 eV) causes an asymmetric distribution in the TSSs and these results are in agreement with the results for helicity-dependent photocurrent in the transport experiments. We extracted the ARPES image and the photoemission dynamics of the TSSs from Ref. [22] and the digitalized figures are shown in Figs. 9(a) and 9(b). Figure 9(a) shows the direct optical transitions from deeper-lying bulk states to the TSSs and the circularly polarized optical pulses result in an asymmetric distribution in the TSSs. Figure 9(b) shows the photoemission dynamics of different positions (1–5) in the TSSs and the relaxation time of the photoemission intensity increases as the position in the TSSs becomes closer to the Dirac point. In Ref. [22], the positions in which energy is less than ~0.3 eV above Fermi level show relaxation properties similar to that of position 5. Therefore, we choose the positions 1–5 for discussion.

The photocurrent density is described by the standard expression, $J = -e\sum_k v_g(k)n(k)$, where k is the momentum state in the band, $v_g(k)$ is the group velocity, and $n(k)$ is the distribution function [28,41,42]. In terms of transient-current radiation, the relaxation time of photoexcited carriers dominates the terahertz emission. Thus, $\partial n(k)/\partial t$ is mainly responsible for the terahertz emission process. Finally, we can simulate the terahertz emission waveforms and spectra from the distribution variation of different states in the TSSs. By taking the far-field diffraction [35,36] into account, the

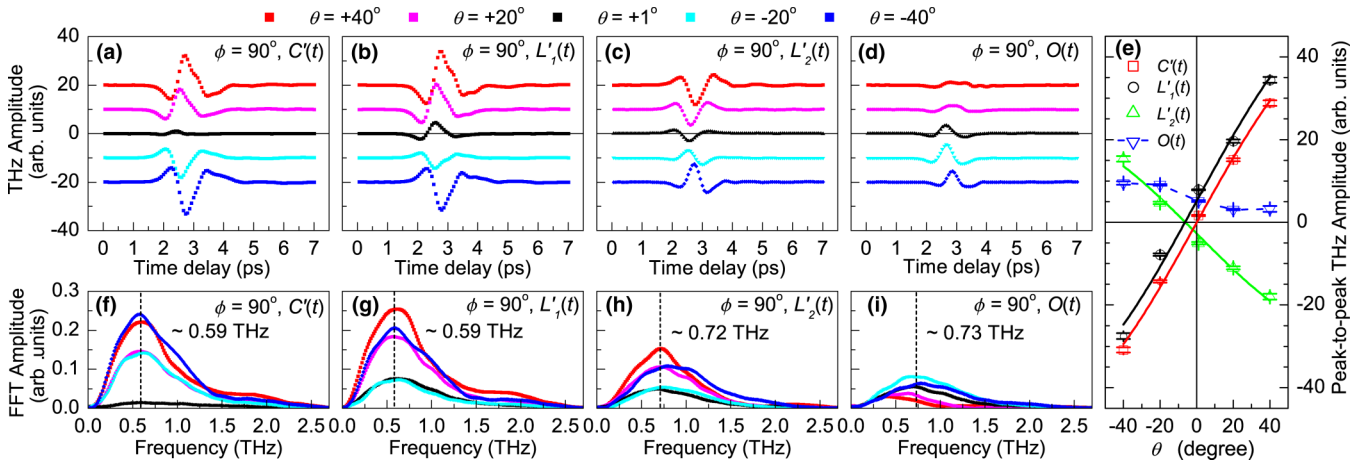

FIG. 8. (a)–(d) The time-domain traces for the coefficients $C'(t)$, $L_1'(t)$, $L_2'(t)$, and $O(t)$ are extracted individually from different α scans [Figs. 7(a)–7(c), $\theta = -40°$, $+1°$, and $+40°$] at $\phi = 90°$. In (b), all extracted time-domain traces for the coefficients $L_1'(t)$ show characteristics similar to that of the coefficients $C'(t)$ in (a). In (c), the polarity of the time-domain traces $L_2'(t)$ is reversed when the sign of the incident angle θ changes. (a)–(d) All of the data are offset to ensure greater clarity. (f)–(i) The corresponding FFT spectra for the time-domain traces in (a)–(d). (f) All of the spectral centers for the coefficients $C'(t)$ are located at 0.59 THz, which coincides with those for the coefficients $L_1'(t)$ in (g). (e) The peak-to-peak values for the time-domain traces shown in (a–d) as a function of the incident angle θ. The red, black, and green lines are the best sinusoidal fits for $C'(t)$, $L_1'(t)$, and $L_2'(t)$, respectively.

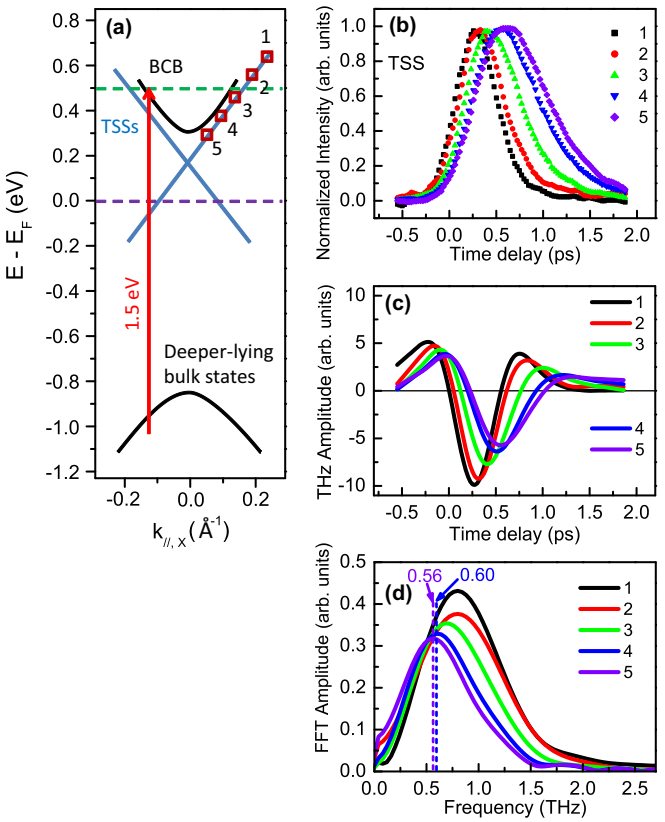

FIG. 9. (a) The schematics for direct optical transitions from deeper-lying bulk states to TSSs in Sb_2Te_3. (b) The normalized photoemission intensities at the different positions (energy-momentum windows described in Ref. [22]) of the TSSs as a function of the pump-probe time delay in the time-resolved ARPES measurements. Both (a) and (b) are digitalized figures that are extracted from Ref. [22]. Considering transient-current radiation with far-field diffraction, the terahertz waveforms and FFT spectra for the contributions from different positions in the TSS are shown in (c) and (d), respectively.

terahertz waveforms from the contributions of the positions 1–5 in the TSSs are obtained and shown in Fig. 9(c). The corresponding FFT spectra are shown in Fig. 9(d). The spectral centers tend toward the low-frequency region as the position becomes closer to the Dirac point. This result agrees with the characteristics of the time-domain photoemission intensity traces. Surprisingly, the spectral centers (0.56–0.60 THz) of the positions 4 and 5 ($E - E_F < 0.3$ eV) are coincident with that of both $C'(t)$ and $L_1'(t)$ for $\phi = 0°$ and 90° in this study. These results provide strong evidence that $C'(t)$ and $L_1'(t)$ originate from TSSs. Nevertheless, all of the positions in the TSSs must be considered (sum over states in the TSSs) for the final terahertz emission. It is noted that most electrons are concentrated in the region near the Dirac point [22] due to the electron bottleneck effect near the Dirac point [32]. Therefore, it is to be expected that the photoexcited carriers near the Dirac point in the TSSs mainly contribute to helicity-dependent terahertz emissioned from a TI Sb_2Te_3 under circularly polarized optical excitations. In general, the filter function of electro-optic sampling (EOS) is necessary to be considered for final terahertz waveforms and spectra. However, the effects of EOS filter function can be neglected due to the flat spectrum in the low-frequency region (<2 THz) [43–45].

Rashba spin-split bulk states would result in spin-polarized photocurrent, and spin-polarized photocurrent may contribute to helicity-dependent terahertz emissions. In general, surface heavy doping and gas absorptions would result in Rashba splitting for the bulk bands. It has been shown that the contribution from Rashba spin-split bulk states in Bi_2Se_3 can be neglected due to the cancellation effect of the two oppositely spin-polarized Fermi surfaces of Rashba bulk bands as well as difficulties for strong band bending without surface doping [11]. For MBE-grown Sb_2Te_3 thin films, it has been shown that the robustness of the TSSs in Sb_2Te_3 is more superior to those in Bi_2Se_3 and Bi_2Te_3 by electrical transport measurements [46]. Furthermore, it has been shown that the aging effect (surface band bending) in Sb_2Te_3 thin films is not obvious, and even the Rashba effect has not been observed by ARPES measurements [47]. This means that strong surface band bending has not been observed in MBE-grown Sb_2Te_3 thin films. Therefore, we believe that the contributions from Rashba spin-split bulk states to CPGE and LPGE can be neglected in our experimental results.

Furthermore, the spectra centers (~0.73 THz) of PDE (dominated by bulk states) all show blueshift with respect to the spectra (~0.61 THz) of CPGE and LPGE. This indicates that terahertz emission spectra from the bulk states are higher than those from TSSs.

APPENDIX F: HELICITY-INDEPENDENT TERAHERTZ RADIATION FROM A ⟨110⟩ ZnTe SINGLE CRYSTAL

To confirm our model, we also use a popular terahertz emitter, a ⟨110⟩ ZnTe single crystal of 1-mm thickness, to

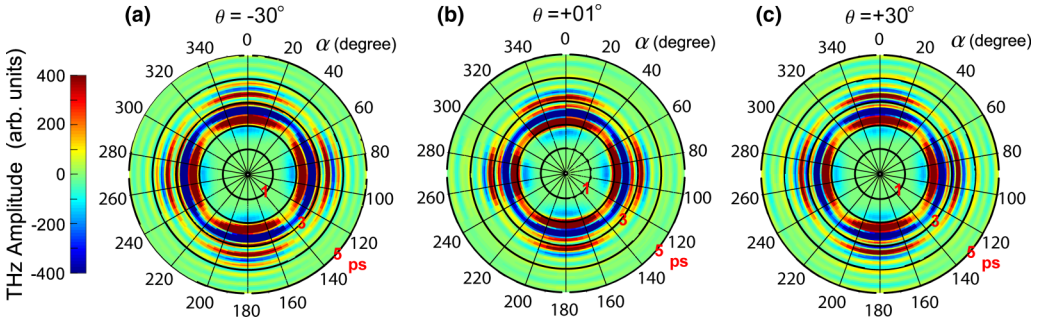

FIG. 10. (a)–(c) α-scan patterns for terahertz waveforms (0–5 ps) from a ⟨110⟩ ZnTe single crystal at $\theta = -30°, +1°$, and $+30°$.

perform an α scan for $\theta = -30^\circ, +1^\circ$, and $+30^\circ$ under the same condition. The mechanism of the terahertz emission from ZnTe is OR. As shown in Fig. 10, apparently, all α-scan patterns show the same 4α periodicity ($\cos 4\alpha$), and no polarity reversal for terahertz waveforms as the incident angle of optical pulses changes from $\theta = -30^\circ$ to $+30^\circ$.

[1] J. E. Moore, Nature **464**, 194 (2010).
[2] M. Hasan and C. Kane, Rev. Mod. Phys. **82**, 3045 (2010).
[3] X.-L. Qi and S.-C. Zhang, Phys. Today **63**, 33 (2010).
[4] Y. L. Chen, J. G. Analytis, J.-H. Chu, Z. K. Liu, S.-K. Mo, X. L. Qi, H. J. Zhang, D. H. Lu, X. Dai, Z. Fang, S. C. Zhang, I. R. Fisher, Z. Hussain, and Z.-X. Shen, Science **325**, 178 (2009).
[5] Y. Xia, D. Qian, D. Hsieh, L. Wray, A. Pal, H. Lin, A. Bansil, D. Grauer, Y. S. Hor, R. J. Cava, and M. Z. Hasan, Nat. Phys. **5**, 398 (2009).
[6] D. Hsieh, D. Qian, L. Wray, Y. Xia, Y. S. Hor, R. J. Cava, and M. Z. Hasan, Nature **452**, 970 (2009).
[7] P. Roushan, J. Seo, C. V. Parker, Y. S. Hor, D. Hsieh, D. Qian, A. Richardella, M. Z. Hasan, R. J. Cava, and A. Yazdani, Nature **460**, 1106 (2009).
[8] T. Zhang, P. Cheng, X. Chen, J.-F. Jia, X. Ma, K. He, L. Wang, H. Zhang, X. Dai, Z. Fang, X. Xie, and Q.-K. Xue, Phys. Rev. Lett. **103**, 266803 (2009).
[9] Z. Alpichshev, J. G. Analytis, J.-H. Chu, I. R. Fisher, Y. L. Chen, Z. X. Shen, A. Fang, and A. Kapitulnik, Phys. Rev. Lett. **104**, 016401 (2010).
[10] S. Kim, M. Ye, K. Kuroda, Y. Yamada, E. E. Krasovskii, E. V. Chulkov, K. Miyamoto, M. Nakatake, T. Okuda, Y. Ueda, K. Shimada, H. Namatame, M. Taniguchi, and A. Kimura, Phys. Rev. Lett. **107**, 056803 (2011).
[11] J. W. McIver, D. Hsieh, H. Steinberg, P. Jarillo-Herrero, and N. Gedik, Nat. Nanotechnol. **7**, 96 (2012).
[12] J. Duan, N.Tang, X. He, Y. Yan, S. Zhang, X. Qin, X. Wang, X. Yang, F. Xu, Y. Chen, W. Ge, and B. Shen, Sci. Rep. **4**, 4889 (2014).
[13] C. Kastl, C. Karnetzky, H. Karl, and A. W. Holleitner, Nat. Commun. **6**, 6617 (2014).
[14] P. Olbrich, L. E. Golub, T. Herrmann, S. N. Danilov, H. Plank, V. V. Bel'kov, G. Mussler, Ch. Weyrich, C. M. Schneider, J. Kampmeier, D. Grützmacher, L. Plucinski, M. Eschbach, and S. D. Ganichev, Phys. Rev. Lett. **113**, 096601 (2014).
[15] J. Tang, L.-T. Chang, X. Kou, K. Murata, E. S. Choi, M. Lang, Y. Fan, Y. Jiang, M. Montazeri, W. Jiang, Y. Wang, L. He, and K. L. Wang, Nano Lett. **14**, 5423 (2014).
[16] K. N. Okada, N. Ogawa, R. Yoshimi, A. Tsukazaki, K. S. Takahashi, M. Kawasaki, and Y. Tokura, Phys. Rev. B **93**, 081403(R) (2016).
[17] T. Kampfrath, M. Battiato, P. Maldonado, G. Eilers, J. Nötzold, S. Mährlein, V. Zbarsky, F. Freimuth, Y. Mokrousov, S. Blügel, M. Wolf, I. Radu, P. M. Oppeneer, and M. Münzenberg, Nat. Nanotechnol. **8**, 256 (2013).
[18] T. J. Huisman, R. V. Mikhaylovskiy, J. D. Costa, F. Freimuth, E. Paz, J. Ventura, P. P. Freitas, S. Blügel, Y. Mokrousov, Th. Rasing, and A. V. Kimel, Nat. Nanotechnol. **11**, 455 (2016).
[19] D. Hsieh, F. Mahmood, J. W. McIver, D. R. Gardner, Y. S. Lee, and N. Gedik, Phys. Rev. Lett. **107**, 077401 (2011).
[20] Y. H. Wang, D. Hsieh, E. J. Sie, H. Steinberg, D. R. Gardner, Y. S. Lee, P. Jarillo-Herrero, and N. Gedik, Phys. Rev. Lett. **109**, 127401 (2012).
[21] M. Hajlaoui, E. Papalazarou, J. Mauchain, G. Lantz, N. Moisan, D. Boschetto, Z. Jiang, I. Miotkowski, Y. P. Chen, A. Taleb-Ibrahimi, L. Perfetti, and M. Marsi, Nano Lett. **12**, 3532 (2012).
[22] J. Sánchez-Barriga, E. Golias, A. Varykhalov, J. Braun, L. V. Yashina, R. Schumann, J. Minár, H. Ebert, O. Kornilov, and O. Rader, Phys. Rev. B **93**, 155426 (2016).
[23] C. W. Luo, H. J. Wang, S. A. Ku, H.-J. Chen, T. T. Yeh, J.-Y. Lin, K. H. Wu, J. Y. Juang, B. L. Young, T. Kobayashi, C.-M. Cheng, C.-H. Chen, K.-D. Tsuei, R. Sankar, F. C. Chou, K. A. Kokh, O. E. Tereshchenko, E. V. Chulkov, Yu. M. Andreev, and G. D. Gu, Nano Lett. **13**, 5797 (2013).
[24] C. W. Luo, H.-J. Chen, C. M. Tu, C. C. Lee, S. A. Ku, W. Y. Tzeng, T. T. Yeh, M. C. Chiang, H. J. Wang, W. C. Chu, J.-Y. Lin, K. H. Wu, J. Y. Juang, T. Kobayashi, C.-M. Cheng, C.-H. Chen, K.-D. Tsuei, H. Berger, R. Sankar, F. C. Chou *et al.*, Adv. Opt. Mater. **1**, 804 (2013).
[25] C.-M. Tu, T.-T. Yeh, W.-Y. Tzeng, Y.-R. Chen, H.-J. Chen, S.-A. Ku, C.-W. Luo, J.-Y. Lin, K.-H. Wu, J.-Y. Juang, T. Kobayashi, C.-M. Cheng, K.-D. Tsuei, H. Berger, R. Sankar, and F.-C. Chou, Sci. Rep. **5**, 14128 (2015).
[26] L. G. Zhu, B. Kubera, K. F. Mak, and J. Shan, Sci. Rep. **5**, 10308 (2015).
[27] J. E. Moore and J. Orenstein, Phys. Rev. Lett. **105**, 026805 (2010).
[28] S. D. Ganichev and W. Prettl, J. Phys. Condens. Matter **15**, R935 (2003).
[29] P. Hosur, Phys. Rev. B **83**, 035309 (2011).
[30] A. Junck, Ph.D. thesis, Freie Universität Berlin, 2015.
[31] R. W. Boyd, *Nonlinear Optics*, 3rd ed. (Academic Press, London, 2008), p. 7.
[32] J. A. Sobota, S. Yang, J. G. Analytis, Y. L. Chen, I. R. Fisher, P. S. Kirchmann, and Z.-X. Shen, Phys. Rev. Lett. **108**, 117403 (2012).
[33] J. Maysonnave, S. Huppert, F. Wang, S. Maero, C. Berger, W. de Heer, T. B. Norris, L. A. De Vaulchier, S. Dhillon, J. Tignon, R. Ferreira, and J. Mangeney, Nano Lett. **14**, 5797 (2014).
[34] H. Plank, L. E. Golub, S. Bauer, V. V. Bel'kov, T. Herrmann, P. Olbrich, M. Eschbach, L. Plucinski, C. M. Schneider, J. Kampmeier, M. Lanius, G. Mussler, D. Grützmacher, and S. D. Ganichev, Phys. Rev. B **93**, 125434 (2016).
[35] J. W. Goodman, *Introduction to Fourier Optics* (McGraw-Hill, New York, 1988) pp. 53–54.
[36] P. Kužel, M. A. Khazan, and J. Kroupa, J. Opt. Soc. Am. B **16**, 1795 (1999).
[37] L. Braun, G. Mussler, A. Hruban, M. Konczykowski, T. Schumann, M. Wolf, M. Münzenberg, L. Perfetti, and T. Kampfrath, Nat. Commun. **7**, 13259 (2016).
[38] S. Y. Hamh, S.-H. Park, S.-K. Jerng, J. H. Jeon, S.-H. Chun, and J. S. Lee, Phys. Rev. B **94**, 161405(R) (2016).
[39] M. Hajlaoui, E. Papalazarou, J. Mauchain, L. Perfetti, A. Taleb-Ibrahimi, F. Navarin, M. Monteverde, P. Auban-Senzier, C. R. Pasquier, N. Moisan, D. Boschetto, M. Neupane, M. Z. Hasan, T. Durakiewicz, Z. Jiang, Y. Xu, I. Miotkowski, Y. P. Chen, S. Jia, H. W. Ji *et al.*, Nat. Commun. **5**, 3003 (2014).

[40] R. Valdés Aguilar, J. Qi, M. Brahlek, N. Bansal, A. Azad, J. Bowlan, S. Oh, A. J. Taylor, R. P. Prasankumar, and D. A. Yarotski, Appl. Phys. Lett. **106**, 011901 (2015).
[41] S. D. Ganichev and W. Prettel, Phys. E (Amsterdam, Neth.) **14**, 166 (2002).
[42] A. Junck, G. Refael, and F. von Oppen, Phys. Rev. B **88**, 075144 (2013).
[43] G. Gallot, J. Zhang, R. W. McGowan, T.-I. Jeon, and D. Grischkowsky, Appl. Phys. Lett. **74**, 3450 (1999).
[44] G. Gallot and D. Grischkowsky, J. Opt. Soc. Am. B **16**, 1204 (1999).
[45] C. M. Tu, S. A. Ku, W. C. Chu, C. W. Luo, J. C. Chen, and C. C. Chi, J. Appl. Phys. **112**, 093110 (2012).
[46] Y. Takagaki, A. Giussani, K. Perumal, R. Calarco, and K.-J. Friedland, Phys. Rev. B **86**, 125137 (2012).
[47] G. Wang, X. Zhu, J. Wen, X. Chen, K. He, L. Wang, X. Ma, Y. Liu, X. Dai, Z. Fang, J.-F. Jia, and Q.-K Xue, Nano Res. **3**, 874 (2010).